November 2022

Orthogonal SAW Biosensor FEM Simulation Based on ST-Quartz with Crystalline ZnO Guiding Layer

Saurabh Patwardhan
University of South Florida

Orthogonal SAW Biosensor FEM Simulation Based on ST-Quartz with Crystalline ZnO Guiding Layer

by

Saurabh Patwardhan

A thesis submitted in partial fulfillment
of the requirements for the degree of
Master of Science
Department of Medical Engineering
College of Engineering
University of South Florida

Major Professor: Venkat Bhethanabotla, Ph.D.
Robert Frisina, Ph.D.
John Kuhn, Ph.D.

Date of Approval:
November 9, 2022

Keywords: Surface acoustic wave (SAW), piezoelectric materials, biofouling, Rayleigh wave, shear-horizontal wave

Dedication

I would like to dedicate this thesis to the sensors team at Bhethanabotla Lab, USF, as well as to my family and friends who supported me tirelessly on this journey towards completing a well-rounded thesis.

Acknowledgments

First, I'd like to acknowledge all the guidance and support from my advisor Dr. Bhethanabotla, who directed me toward the exploration of guiding layer configurations. I would also like to thank Mr. Pradipta Das who tirelessly helped me work on the problem, providing me with invaluable tools and support every step of the way.

I would also like to acknowledge all the research computing help from Mr. John DeSantis and Dr. Tony Green, as well as others whom I worked with indirectly.

Table of Contents

List of Tables

List of Figures

Abstract

Detection of trace amounts of biomarkers is a critical requirement in sensing the presence of conditions such as early-stage cancer. The ST cut of the Quartz crystal (ST-Quartz) supports two fundamental surface acoustic waves (SAWs) in mutually perpendicular, or orthogonal, directions: the Rayleigh wave and the shear-horizontal wave (RSAW and SH-SAW, respectively). The orthogonality enables the use of ST-Quartz in biofouling removal by the RSAW and mass sensing via the SH-SAW simultaneously. The purpose of this study is to find an ideal guiding layer and wavelength configuration that can enhance the sensing capability without sacrificing the biofouling removal ability for a biosensor.

Finite-element modeling (FEM) has been used to predict the behavior of complex materials with fair reliability. First, the resonant frequency of the Love mode (which is a layer-guided SH-SAW) will be determined for a certain thickness of ZnO guiding layer via the transient analysis of its impulse response. Then, the thickness and frequency data will be used to create a perturbation-theory-based steady-state analysis model that calculates sensitivity of the configuration. Once the optimal guiding layer thickness has been found from the first two points above, different configurations of the RSAW transducers can be explored to maximize kinetic energy on the surface, or in this case, voltage and displacement power, using FEM.

From preliminary results, the Love wave and RSAW models were confirmed to be reliable by verifying wave velocity and nodal displacement profiles with previously reported data. The sensitivity results were plotted against the ZnO guiding layer thickness. Love wave models with different wavelengths were found to have distinct sensitivity peaks, indicating the presence of an

optimal thickness. For the ZnO/ST-Quartz configuration, the optimal thickness for the Love wave was found to be a ratio of approximately 0.035 of layer thickness/wavelength. The RSAW model was tested with two IDT configurations: one with the IDTs below the guiding layer and another with IDTs above the guiding layer. Similar to the Love wave simulations, a peak power was observed in the RSAW models for a ZnO layer thickness/wavelength ratio of approximately 0.4.

Some drawbacks of these models include the crystal rotation mathematics, which assume a cubic nature of crystals; variability of material properties in practical applications; and the simplified nature of the FEM in comparison with actual devices.

Chapter 1: Introduction and Literature Review

In this Chapter, a brief introduction to acoustic sensors leads into a discussion of surface acoustic wave (SAW) devices, followed by applications of SAWs. In this work, a layer-guided orthogonal SAW device, specifically ZnO/ST-Quartz, is simulated to test the feasibility and explore an optimal design. Subsections 1.1–1.2 introduce SAW devices; Subsection 1.3 introduces the concept of biofouling and its mitigation strategies; and Subsections 1.4–1.5 establish the basis for layer-guiding orthogonal SAW devices. Chapter 2 introduces the materials and establishes a mathematical basis for testing the models in ANSYS.

1.1 Acoustic Wave Devices

Acoustic sensors typically operate with physical vibrations in a medium, which may interact with an analyte. These interactions cause a change in the characteristics of vibration, which can then be quantified and used for sensing the analyte [1]. Acoustic waves are actuated in piezoelectric materials, such as Quartz (crystal of SiO_2) or single-crystal $LiNbO_3$, by means of electrical energy being transduced to and from mechanical strain energy [2]. Acoustic sensors are broadly classified per their mode of vibration: bulk acoustic wave (BAW), flexural plate wave (FPW), SAW sensors, etc.

1.2 Surface Acoustic Waves (SAWs)

SAWs are acoustic perturbations that are confined to the surface of a piezoelectric crystal. SAWs have long been documented in piezoelectric materials, and they can be used for many applications, such as biosensing, gas sensing, nebulization, and radio-frequency (RF) filtering [3][4]. Typically actuated with interdigitated transducers (IDTs), SAWs can be classified in

different types depending on their mode of propagation, wave speed, and interaction with any modifications to the crystal surface. An example of a SAW model with IDTs is shown in Figure (1.1). The different modes of SAWs can be utilized for various applications. For example, the Rayleigh mode (RSAW) and its harmonics are suitable for RF filtering [5] or gas sensing [6] since it has lower signal loss, whereas surface transverse waves (STWs) can be better suited for biochemical sensing. For sensing, having a larger portion of energy confined to the surface is desirable, which is the case of both STWs and RSAWs [1][7]. In addition, liquid media interact more with RSAWs than with STWs; in case of blood-based samples, appropriately functionalized STW devices would interact more specifically with analytes than the blood medium itself. Therefore, STWs are more suitable for detecting target analytes in liquid media via capture functionalization for a target analyte.

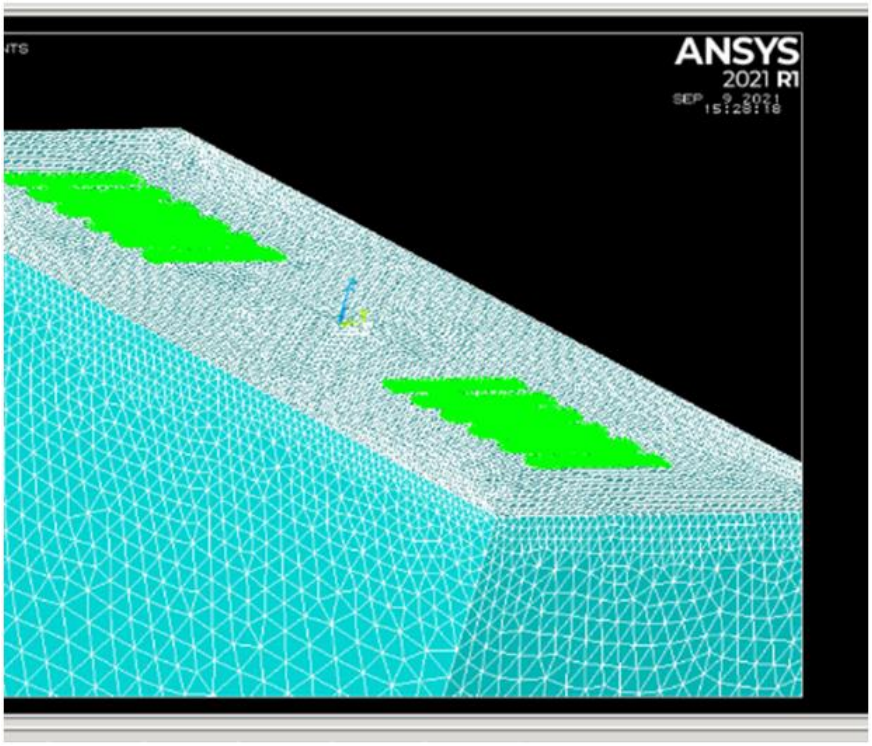

Figure 1.1 A model of the bare ST-Quartz chip, with interdigitated transducers (IDTs) in green.

1.3 Biosensing and Biofouling

In serological testing, the detection of trace amounts of antigens is a critical requirement in quantifying biomarkers of conditions such as early-stage cancer [8]. For doing so, biosensors are often employed to identify such markers, with a wide range of operating principles. In most applications, the antibody–antigen binding strategy is employed, due to the extremely high specificity of this binding [9]. In such strategies, a testing surface is functionalized by coating with capture antibodies, which specifically bind to the target antigen analyte. Acoustic wave biosensors have adopted similar strategies, with bulk acoustic wave (BAW) biosensors being commonly used in the shear-horizontal modes. SAW devices operating in similar modes are a plausible alternative for such BAW devices [10].

Although the specificity of antibody–antigen binding is high, many biosensors face the problem of biofouling, whereby undesired proteins and/or epitopes weakly bind with the capture antibodies via electrostatic interactions and van der Waals forces. Such bindings undermine the detection specificity of a biosensor [11]. Hypothetically, a large amount of biofouling by non-target entities can elicit the same response as that by a small amount of target entities, which may result in false-positive readings. Therefore, mitigating biofouling is crucial, especially in sensors that are designed to reliably detect trace amounts of an analyte.

1.4 Rayleigh Streaming and Its Application in Biofouling Removal

When a Rayleigh wave encounters a liquid medium on the surface, it interacts with that medium. The wave in the substrate loses energy the further it travels along the medium interface, and it diffuses that energy as pressure waves in the liquid. This phenomenon is termed as acoustic streaming, and streaming has been explored for its potential to mitigate biofouling [12]. With biofouling, non-target entities weakly bind to the bioreceptors, hereafter termed as non-specific

binding (NSB). With appropriate Rayleigh streaming, the NSB energy can be overcome with lift and drag forces to effectively reduce biofouling. Previously, a langasite-based sensor was theorized that could simultaneously conduct sensing and biofouling removal using the orthogonal functionality of the langasite crystal [13]. Based on the same concept, this work explores the possibility of a layer-guided orthogonal SAW sensor using an ST-Quartz substrate and ZnO guiding layer.

1.5 Orthogonal Functionality of ST-Quartz

The ST cut of the Quartz crystal (ST-Quartz) supports two fundamental SAWs in orthogonal directions: the Rayleigh wave and the shear-horizontal wave (Figures 1.2(a) and (b), RSAW and SH-SAW, respectively) [14]. The orthogonal propagation of these two waves enables one to design sensors that can simultaneously use these two modes for different purposes: the RSAW has been documented to be capable of mitigating biofouling [15], whereas the SH-SAW has been used in sensing applications. The two wave modes have been illustrated for the ST-Quartz substrate in Figure (1.2).

1.6 Waveguides in SAW Devices

A drawback of orthogonal sensors is that the sensitivity of SH-SAW is not suitable for detecting trace amounts of antigens, and they usually require guiding layers to improve the sensitivity. Waveguides are thin layers of functional materials on a substrate. In case of SAW devices, some waves are classified as “leaky,” wherein SAWs aren’t strictly confined to the surface but propagate slightly towards the depth (or negative *z*-direction) [4]. An example of such a leaky mode is the SH-SAW in ST-Quartz and other materials. A waveguide helps confine the energy of such leaky modes to the surface via refraction [16]. An effective waveguide for leaky SAWs has a lower wave speed in the guiding layer than that in the substrate.

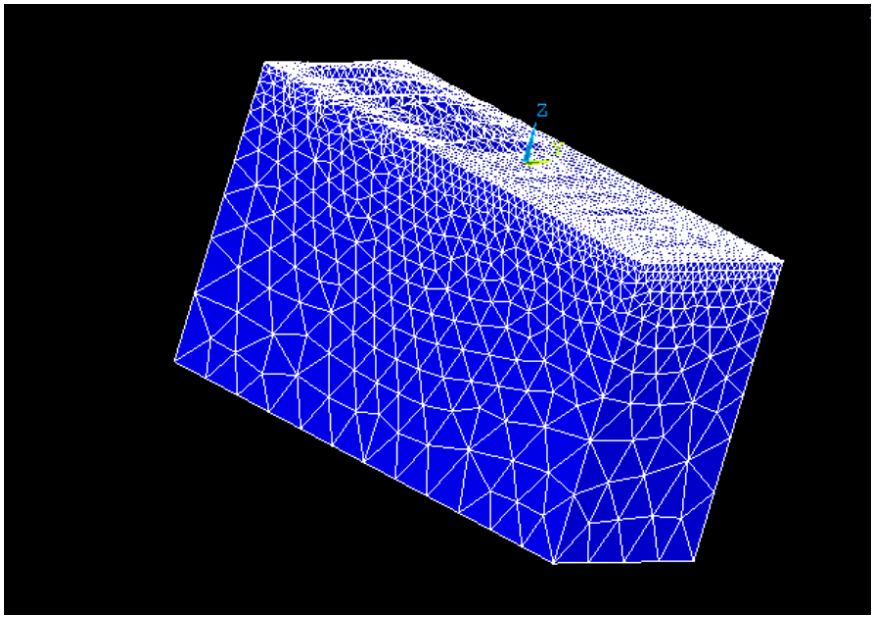

(a)

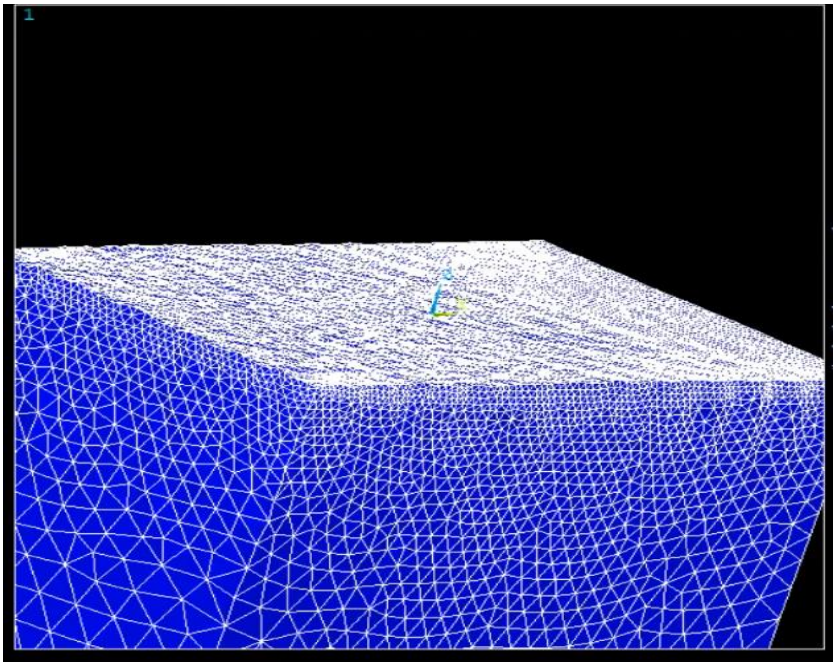

(b)

Figure 1.2 Shown are simulations of (a) Rayleigh and (b) shear-horizontal surface acoustic wave modes (RSAW and SH-SAW modes, respectively), on orthogonal orientations of an ST-Quartz crystal. The RSAW has significant out-of-plane vibrations (Z-direction in (a)), whereas the SH-SAW has minimal out-of-plane vibrations.

In general, adding a layer of waveguiding material helps improve the signal strength and increase the sensitivity of SH-SAW sensors. Such a mode of vibration, a layer-guided SH-SAW, is referred to as the Love wave [17].

1.7 Waveguiding Orthogonal SAW Devices

In ST-Quartz, SiO_2 and ZnO thin films have been empirically shown to improve the sensitivity of the SH-SAW mode [18][19]. However, adding a guiding layer in such an orthogonal device would possibly weaken the RSAW energy due to damping. Thus, to create a functional orthogonal layer-guided device, certain modifications must be explored to overcome the RSAW damping effect. These modifications may include increasing the operational frequency in order to reduce the absolute thickness of the guiding layer, or actuating the RSAW from a piezoelectric guiding layer such as ZnO.

1.7.1 Increasing the Operational Frequency

One approach for a functional layer-guided orthogonal device would be to increase the resonant frequency of the Love mode. The optimal thickness of the guiding layer is proportional to the wavelength of a mode [20], and therefore inversely proportional to the frequency. Therefore, a high-frequency device will need a thin guiding layer, and the thinner the layer, the lower the damping of the RSAW. However, a higher frequency presents difficulties in fabrication, as the transducer geometry scales down in size with increasing frequency. Operational frequencies of Love wave devices are typically in the range of 80–300 MHz [21].

1.7.2 Actuating Rayleigh SAW (RSAW) from Guiding Layer

A second approach would be to use a guiding layer material that is itself capable of actuating RSAW, in which case the problem of the guiding layer damping the substrate's RSAW becomes irrelevant.

In theory, any piezoelectric material with a large d_{33} coefficient, which is associated with out-of-plane vibration, is capable of actuating RSAW [22], such as AlN and ZnO [23][24].

1.8 Finite-Element Modeling (FEM) of Orthogonal Devices

Finite-element modeling (FEM) has been used to predict the behavior of complex materials with fair reliability. Previous models for examining sensitivity have used nodal displacement and voltage data that were applied into perturbation theory formulae [25][26]. However, the equations used in these studies were changed significantly to accommodate the fairly simple FEM (with only nodal displacement and voltage data). Current ANSYS models can provide elemental energy as well as velocity solutions, due to which the need to modify the original equations is eliminated. In this study, the primary aim is to predict the optimal orthogonal configuration of an ST-Quartz device with a ZnO guiding layer using ANSYS. The overall approach is to first determine the ideal thickness of the Love wave for maximum sensitivity for different wavelengths, and then to obtain the best configuration of RSAW transduction for the optimum thicknesses.

1.8.1 Sensitivity Analysis

For sensitivity analysis, the resonant frequency of the Love mode will be determined for a certain thickness of ZnO via transient analysis of an impulse response. Then, the thickness and frequency data will be used to create a perturbation-theory-based steady-state analysis model [26], which may be used for calculating the sensitivity of the configuration.

1.8.2 RSAW Analysis

Once the optimal guiding layer thickness has been found from the two models above, different configurations of the RSAW transducers for the optimal guiding layer thickness can be explored to maximize kinetic energy on the surface. The effect of changing the wavelength of the RSAW as well as positioning of the interdigitated transducers (IDTs) below and above the guiding

layer can be examined. To the best of our knowledge, the use of a ZnO guiding layer on an orthogonal ST-Quartz chip has not been explored yet.

Chapter 2: Methods, Materials, and Governing Equations

In this Chapter, the basis theory for modeling the simulations is described, as well as the equations to be used for analyzing sensitivity of the Love mode. To ascertain the optimal configuration of the orthogonal sensor, the aim of the simulations is designed in two steps: the first step is to determine peak sensitivity of the device as a function of the guiding layer thickness. The next step would be to test various RSAW transducer designs to compare biofouling functionality. An optimal configuration would be defined as that which provides maximum sensitivity as well as high biofouling-removal ability.

2.1 Perturbation Theory

For determining the sensitivity of a Love wave configuration, perturbation-theory-based equations may be used. Perturbation theory was first used to mathematically explain the behavior of SAW sensors under mass loading by Auld [27]. Several researchers extended this work to include different aspects of SAW devices. For example, Wang et al. [28] published sensitivity equations for planar multilayered acoustic sensors. Based on Wang et al.'s equation, the following formulation (Equation (1)) may be used along with FEM data to calculate sensitivity:

$$\frac{\Delta f}{f_0} = \frac{-\rho_m \varepsilon}{4U_a}\left[|v_x|^2 + |v_y|^2 + |v_z|^2\right] \quad (1)$$

Here, ρ_m [g cm^{-3}] is the density of the added analyte that is assumed to be in the form of a layer; ε [cm] is the thickness of the hypothetical layer; v_i [cm s^{-1}] is the average velocity of the nodes in the *i* direction on a selected area on the top surface; U_a [J cm^{-2}] is area average of total wave energy under that area on the surface. For a Love wave sensor, the velocity and displacement of any point is highest in the direction along the surface plane that is perpendicular to the direction

of propagation. In this case, the direction of propagation is *y*, whereas the *z* direction is out-of-plane with respect to the surface; therefore, the *x*-direction velocity and displacement will be the highest. Hence, v_y and v_z can be neglected. Additionally, if mass loading is rewritten as $\rho_m \Delta\varepsilon \approx \Delta m$ [g/cm^2], we can rearrange the sensitivity equation as Equation (2) below:

$$S_m^f = \frac{1}{f_0} \lim_{\Delta m \to 0} \left(\frac{\Delta f}{\Delta m}\right) = -\frac{|v_x|^2}{4U_a} \tag{2}$$

Velocity of surface nodes, v_x, and the wave energy average, U_a, can be obtained from the nodal solutions of ANSYS structural simulations. The resonant frequency f_0 can be derived from impulse-response testing.

2.1.1 Resonant Frequency

For determining the resonant frequency (f_0) for a SAW model, impulse-response testing was employed in this work, which is a form of transient analysis. The impulse response in this work elucidates time-domain displacement and voltage profiles of desired nodes. These time-domain profiles were then converted to their frequency domain, for plotting the frequency distribution of voltage and displacement at a specific node. Sampling frequencies for all impulse response tests were about 20 times higher than the expected center frequency, in part to obtain a high-resolution waveform and additionally to look for harmonics, if any.

Table 2.1 Sampling parameters for Love wave modeling.

Wavelength (um)	Operational Frequency (MHz)	Sampling frequency (MHz)	Testing period (ns)	Time step (ns)
20	255	5000	50	0.2
40	127.5	2500	100	0.4
60	85	1666.67	150	0.6
80	63.75	1250	200	0.8

For example, the sampling frequency of the 20-micron wavelength model was set to 5 GHz, when the expected center frequency was approximately 250 MHz. This yielded a Nyquist ratio of 20 for the fundamental frequency, and a reasonable upper limit of 2.5 GHz for harmonics.

2.1.1.1 Impulse Response

Impulse response testing is used in various fields ranging from construction [29] to sensors [30] for plotting the vibrational or electrical frequency response of devices, structures, etc. The basis of this testing is to understand the distribution of frequencies in response to a brief and sharp input signal (which is termed as an impulse). For transducers, the impulse signal and response frequency can be in different forms of energy, such as an electrical signal created by a microphone in response to an input acoustic signal. In case of piezoelectric sensors, electrical energy is transformed to and from mechanical stresses in a piezoelectric crystal.

As mentioned previously, for a Love wave, the displacement is predominantly in the *x*-direction if the direction of propagation is *y*. Meanwhile, for a Rayleigh wave sensor, the displacement is predominantly in the *z*-direction. The *z*-direction is out-of-plane from the sensor's surface. The displacement in RSAW is secondarily in the direction of propagation (which is the *x*-direction in this case), whereby the Rayleigh wave creates an elliptical path.

2.1.1.2 Spectral Analysis

Impulse-response testing results in time-domain voltage and displacement plots for a particular model. The resonant frequency is then plotted using spectral analyzers that convert the time-domain displacement data to the frequency domain. Initially, a fast-Fourier transform (FFT) function was used for conversion; however, this resulted in poor resolution of the plot (Figure (2.1)). Ideally, a smoother plot was desired, and an FFT function was unsuitable for that purpose. Therefore, a power spectrum function, "pspectrum" in MATLAB, was considered. The spectral

plots obtained from the power spectrum function was much smoother, and they had much more customizability (Figure (2.2)).

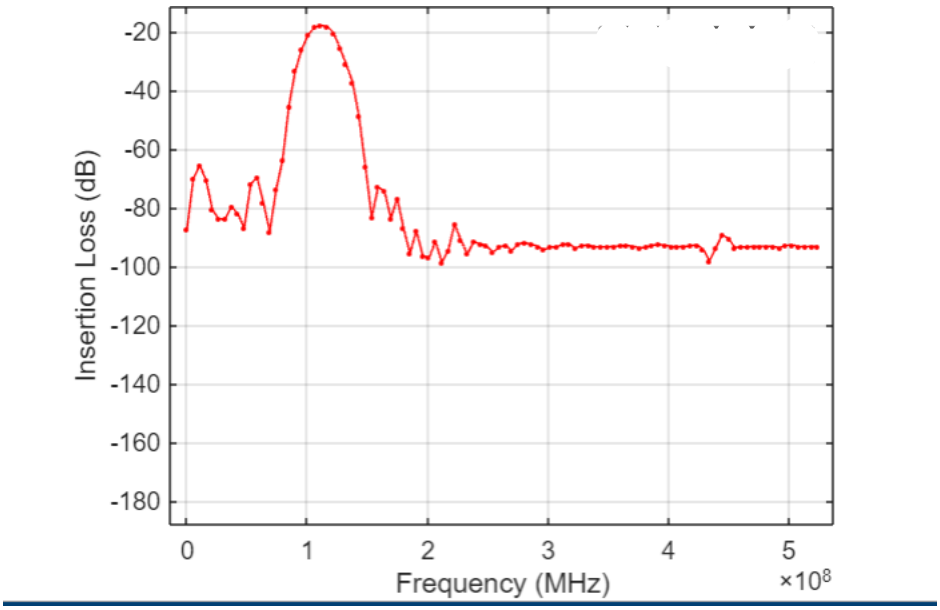

Figure 2.1 A plot of insertion loss [dB] of a ZnO/ST-Quartz chip, using a fast-Fourier transform function (FFT).

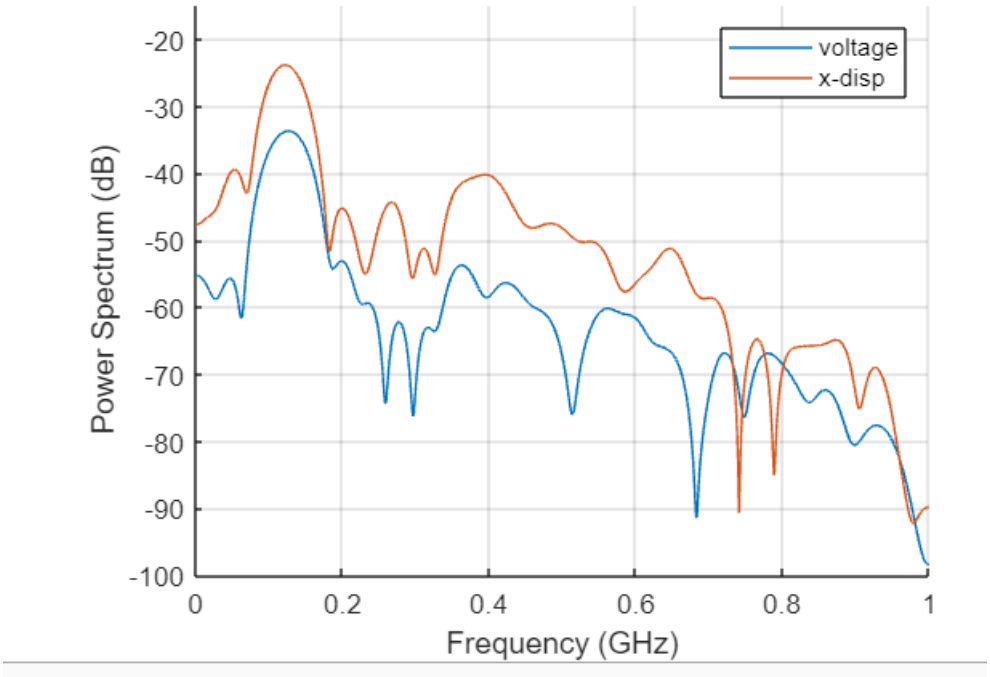

Figure 2.2 A plot of power spectrum [dB] of a ZnO/ST-Quartz chip, with the "pspectrum" command in MATLAB. The orange plot is the frequency-domain response of *x*-displacement, which coincided with the voltage plot in blue, as expected for a Love-wave device.

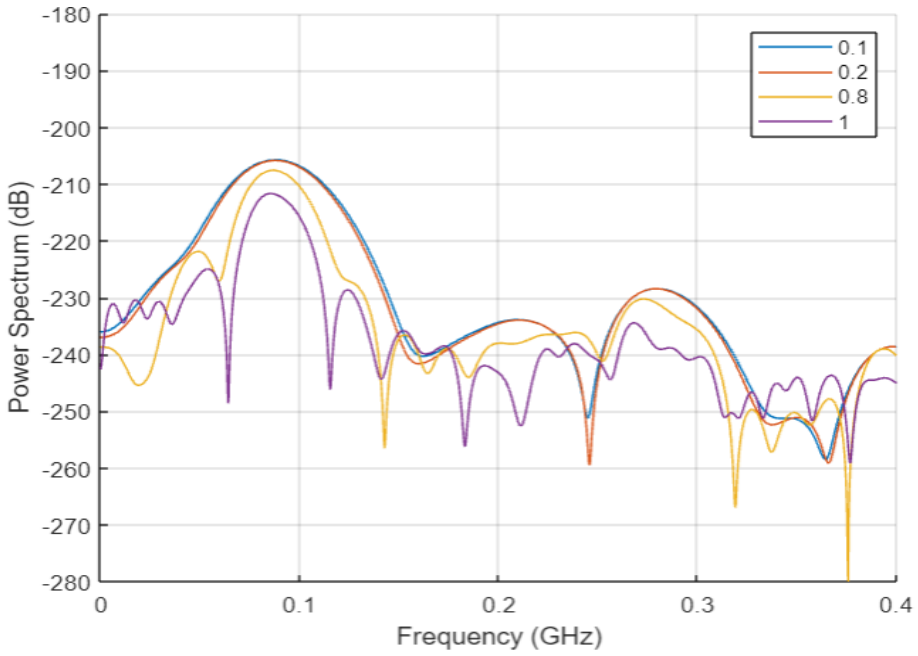

Figure 2.3 A plot of power spectrum [dB] of a ZnO/ST-Quartz chip, with variable windowing parameter values, called leakage. The legend shows the values of leakage.

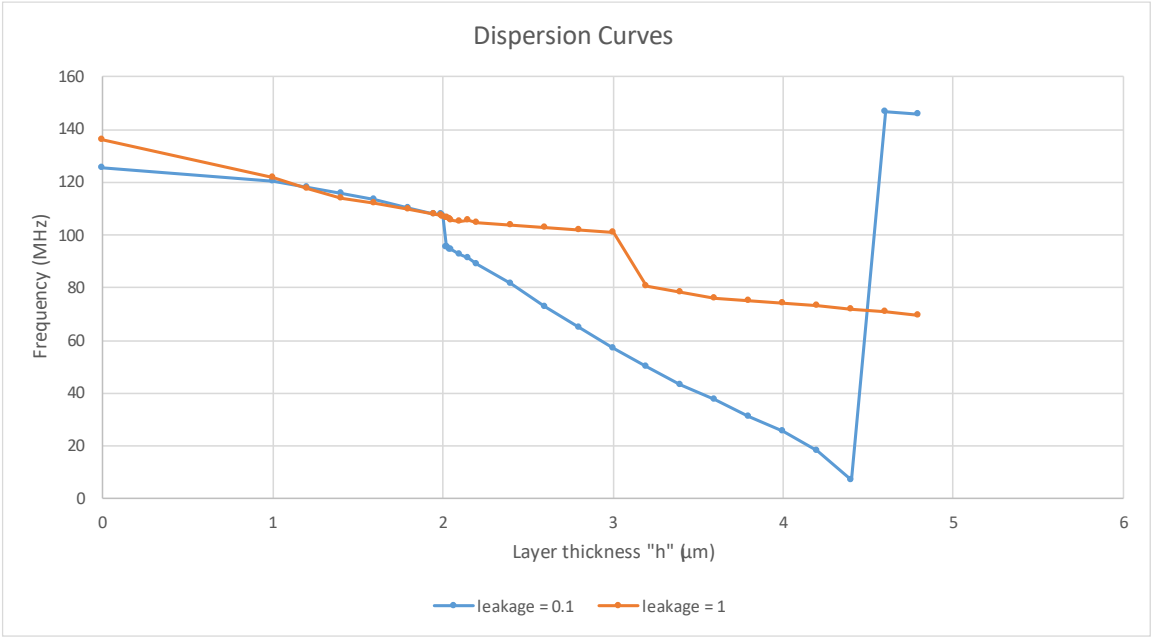

Figure 2.4 An example of "jumps" in resonant frequency with extreme leakage parameters. For the "pspectrum" command, leakage varies from 0 to 1. The orange plot is dispersion curve of *x*-displacement with leakage = 1, whereas the blue plot is with leakage = 0.1.

Figure (2.3) shows the different spectra for the same set of data with different values of leakage, which is a sampling window parameter. Lower leakage values corresponding to broader sampling windows and higher values corresponding to narrow ones. Higher leakage values have better ability to resolve separate peaks, but with added side lobes (for more information, refer to https://www.mathworks.com/help/signal/ref/pspectrum.html). With this function, controlling the windowing parameter (leakage, in this case) was essential: too high or too narrow windows resulted in drastic changes or "jumps" in resonant frequency for small changes in guiding layer thickness (Figure 2.4). With a leakage of 0.8 combined with a peak search function, a reasonably smooth resonant frequency versus guiding layer thickness plot (also known as a dispersion curve) was obtained for the same dataset (Figure 2.5).

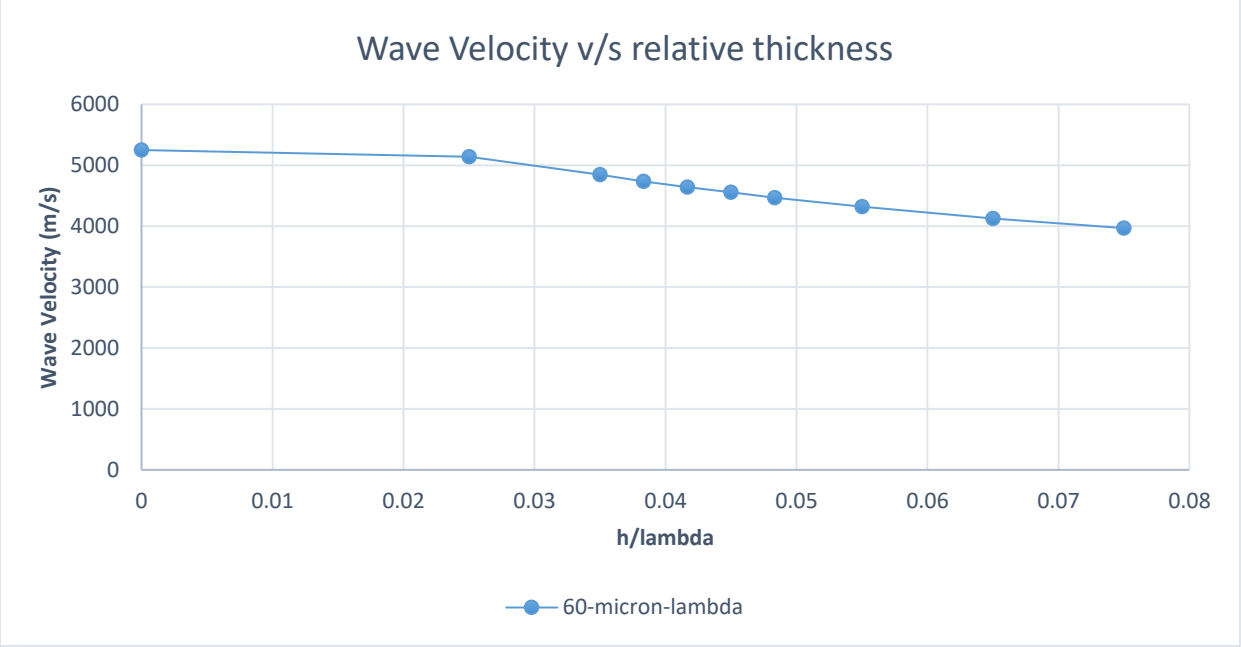

Figure 2.5 An example of a smooth dispersion curve with a moderate leakage parameter (0.8). The blue plot is dispersion curve of *x*-displacement for a 60-micron-wavelength ZnO/ST-Quartz device with varying guiding layer thicknesses (represented by h/lambda on the *x*-axis).

2.1.2 Steady-State Analysis

After the resonant frequency (f_0 in Equation 2) of a Love wave device is determined, the sensitivity of the device at that frequency is calculated. To that end, steady-state testing is preferred over impulse-response testing for two reasons: 1) it focuses on obtaining the response of a device at a very specific frequency instead of the whole spectrum, and 2) in empirical tests for sensitivity, vector network analyzers (VNAs) are employed, which generally use a version of steady-state analysis (e.g., chirp-response testing in the S5045 VNA by Copper Mountain Technologies® used by our lab) as opposed to a true impulse response. Steady-state analysis for Love wave devices involves the observation of velocity and energy of the crystal in response to an input alternating current (AC) signal at its resonant frequency, f_0.

2.2 Materials and Crystal Rotations

In this section, the rationale for choosing Quartz and ZnO has been mentioned, as well as an explanation about their rotations and possible alternative materials. For orthogonal SAW functionality, a crystal must be able to support two surface wave modes propagating perpendicular to each other. Examples of such crystals are Langasite [14] and ST-Quartz. The Quartz crystal supports different wave modes depending on its crystal orientations, many of have been discovered and applied for purposes such as RF filtering [31] and sensing [32].

Sensor configurations with a ZnO guiding layer on ST-Quartz substates have been extensively studied, possibly owing to the positive temperature coefficient of frequency (TCF) of ST-Quartz being balanced out by the negative TCF of ZnO [18]. ZnO also is a strong piezoelectric material, capable of generating fundamental RSAW as well as higher order Sezawa modes with appropriate substrates [33]. A piezoelectric ZnO layer can thus serve to actuate RSAW depending on the thickness, crystal orientation, and the substrate material [34][35].

2.2.1 Crystal Rotations

Quartz and sputtered crystalline ZnO are anisotropic materials; therefore, a change in crystal orientation inevitably leads to a change in the physical properties. In this work, the ZnO guiding layer is assumed to be sputtered onto an ST-Quartz substrate in its c-axis orientation, and the material properties for such a layer have been published previously. The Quartz substrate is considered to have the ST-cut; hence, the material properties of Quartz need to be changed to suit the ST-cut.

The mathematics involved in the rotation of the elastic and piezoelectric matrices was explained by Bond in 1943 [36]. Considering three rotation angles (φ, θ, ψ) about the *z*-, *x*-, and *z*-axes, respectively, the rotation matrix R was defined therein as follows, in Equation (3).

$$R = \begin{pmatrix} \cos\psi & \sin\psi & 0 \\ -\sin\psi & \cos\psi & 0 \\ 0 & 0 & 1 \end{pmatrix} \cdot \begin{pmatrix} \cos\theta & 0 & -\sin\theta \\ 0 & 1 & 0 \\ \sin\theta & 0 & \cos\theta \end{pmatrix} \cdot \begin{pmatrix} \cos\varphi & \sin\varphi & 0 \\ -\sin\varphi & \cos\varphi & 0 \\ 0 & 0 & 1 \end{pmatrix}$$

or

$$R = \begin{pmatrix} \cos\psi\cos\theta\cos\varphi - \sin\varphi\sin\psi & \sin\varphi\cos\theta\cos\psi + \cos\varphi\sin\psi & -\sin\theta\cos\psi \\ -\cos\psi\cos\theta\sin\varphi - \sin\varphi\cos\psi & -\sin\varphi\cos\theta\sin\psi + \cos\varphi\cos\psi & \sin\theta\sin\psi \\ \cos\varphi\sin\theta & \sin\varphi\sin\theta & \cos\theta \end{pmatrix} \cdot \tag{3}$$

This rotation matrix, R, is applicable for vector geometry, wherein the directional information is represented by a 1 × *n* matrix. For example, the unit vectors for a velocity can be represented in a 1 × 3 matrix in 3D space, such as [***i***, ***j***, ***k***]. However, for tensor geometry, directional information is often represented by *n* × *n* or higher-rank matrices. For example, for a strain tensor, longitudinal and shear forces have unique directions due to a mixture of translational and rotational interactions. Thus, the directional information is stored in a 3 × 3 matrix. In the case of the stiffness matrix of an anisotropic material, the full tensor is in a 3 × 3 × 3 × 3 form. However,

not all elements in that matrix are independent, and owing to matrix symmetry, the number of independent elements round down from 81 to a maximum of 21 [37]. These 21 stiffness elements are notated in a 6 × 6 triangular matrix, usually adopting the Voigt notation [38]. Similarly, the piezoelectric matrix coefficients round down from a 3 × 3 × 3 tensor to a 6 × 3 Voigt notated matrix. To accommodate for spatial rotations in higher order matrices, the rotation multiplication equations were published by Auld in the seminal 1973 work on acoustic waves in solids [27]. These Voigt-notated matrices needed to be converted into their standard notations for ANSYS, which required slight rearrangement of both the stiffness and piezoelectric coupling matrices. An example of such a conversion is shown below (Figure (2.6)).

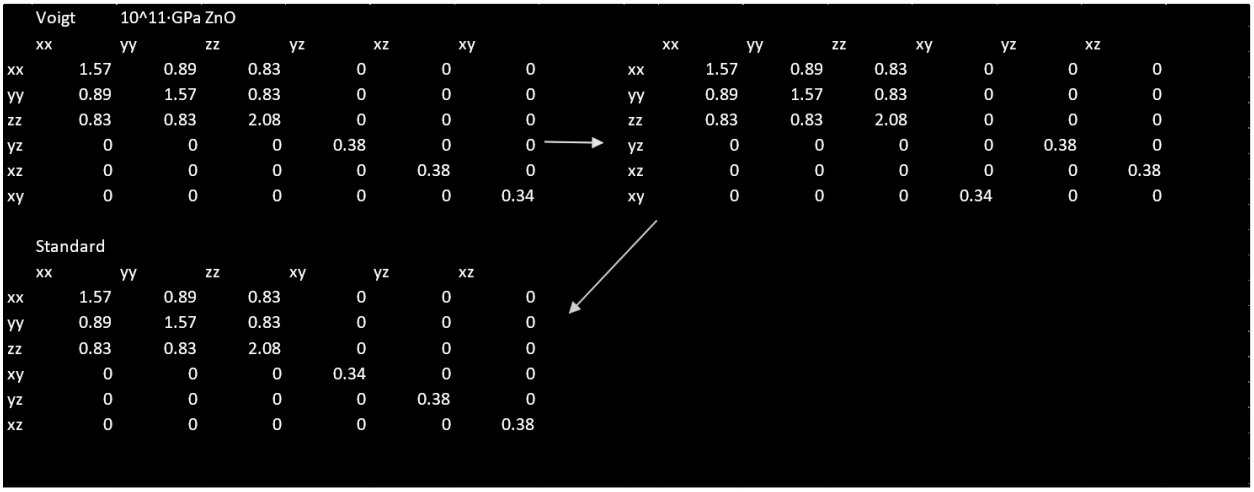

Figure 2.6 Top left 6×6 matrix shows the Voigt-notated stiffness matrix [10^{11} GPa]. The bottom left matrix is the same stiffness matrix in its standard notation.

2.2.2 ST-Quartz

The α-Quartz crystal (hereafter simply Quartz crystal) is a trigonal crystal composed of SiO_2 in a tetrahedral pattern. It is known to be piezoelectric, and it has anisotropic material properties [39]. Different orientations or cuts of the Quartz crystal have been researched for various

applications, such as temperature-stable cuts [31]. Temperature-stable cuts help fabricate devices with low TCFs, improving their operating range of temperatures.

In this work, the ST-cut Quartz orientation was employed (hereafter ST-Quartz). The Euler angles used for rotating the crystal orientation were (0°, 47.25°, 0°), for *y*-propagating RSAW and *x*-propagating SH-SAW. The elastic constants for Quartz were acquired from Heyliger et al.'s work [40], whereas the piezoelectric coupling and the permittivity matrices were obtained from Silva and Santos's work [41].

2.2.3 Zinc Oxide

Zinc Oxide is a naturally occurring compound in the form of the mineral zincite. In its amorphous form, it is a white powder or a colorless solid. ZnO crystallizes preferably in the hexagonal wurtzite structure [42]. Zinc Oxide films have been widely studied for their various applications in SAW and other piezoelectric and acousto-optic devices. Carlotti et al. conducted an acoustic investigation of the physical properties of RF-sputtered ZnO layers, and compared the properties to those of bulk ZnO [43]. In this work, the material properties reported by Carlotti et al. were used for the simulations. In the Love wave simulations, the anisotropic stiffness matrix of ZnO was used but the piezoelectric coupling matrix was nullified. The reason for doing so was to avoid any acoustic waves actuated by the ZnO layer interfering with the guided SH-SAW from the Quartz, possibly skewing the elemental energy profiles (as discussed in Chapter 2.1.2) with an increasing thickness of the ZnO layer. The ZnO piezoelectric coupling was reinstated for RSAW simulations.

Chapter 3: Results and Discussion

This Chapter is divided into three parts: 1) Preliminary results that establish the reliability of the model, 2) Love wave simulation results and discussion, and 3) RSAW simulation results and discussion.

3.1 Preliminary Results

3.1.1 Impulse Voltage

A preliminary model was created with the bare ST-Quartz device, and an impulse voltage was applied to alternate IDTs on one side of the device. Figure (3.1) shows the voltage profile of a node near the Cartesian origin. The impulse voltage can be visualized in the former figure as a short sharp spike in the beginning.

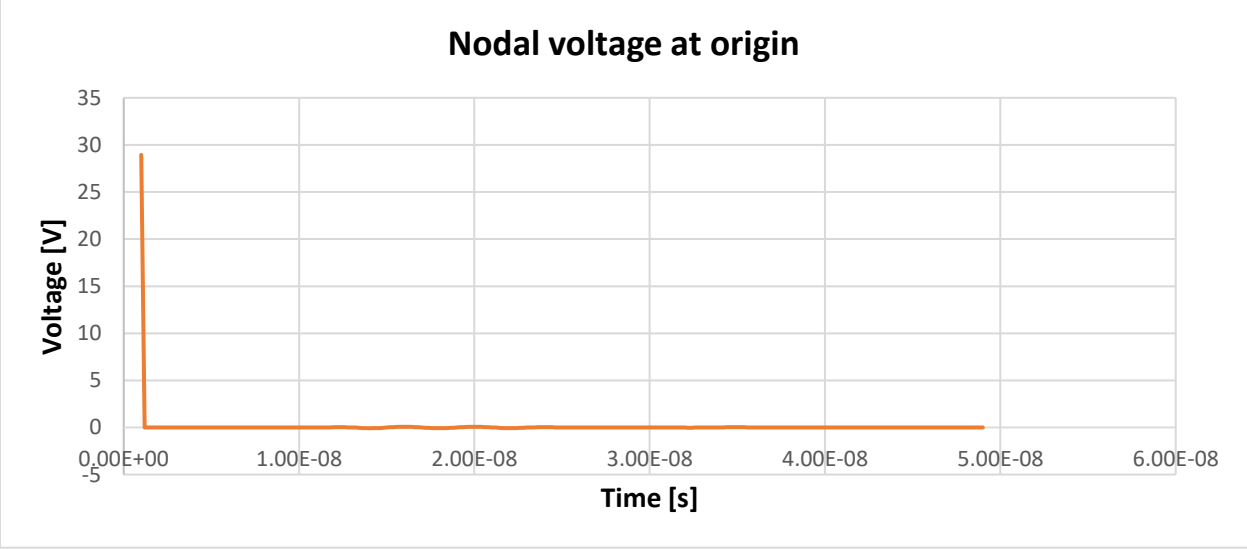

Figure 3.1 Voltage profile of a node near the Cartesian origin of a bare ST-Quartz crystal. The sharp peak in the beginning indicates an impulse voltage.

3.1.2 Displacement Profiles

Figures (3.2a) and (3.2b) show the displacements of a node near the Cartesian origin.

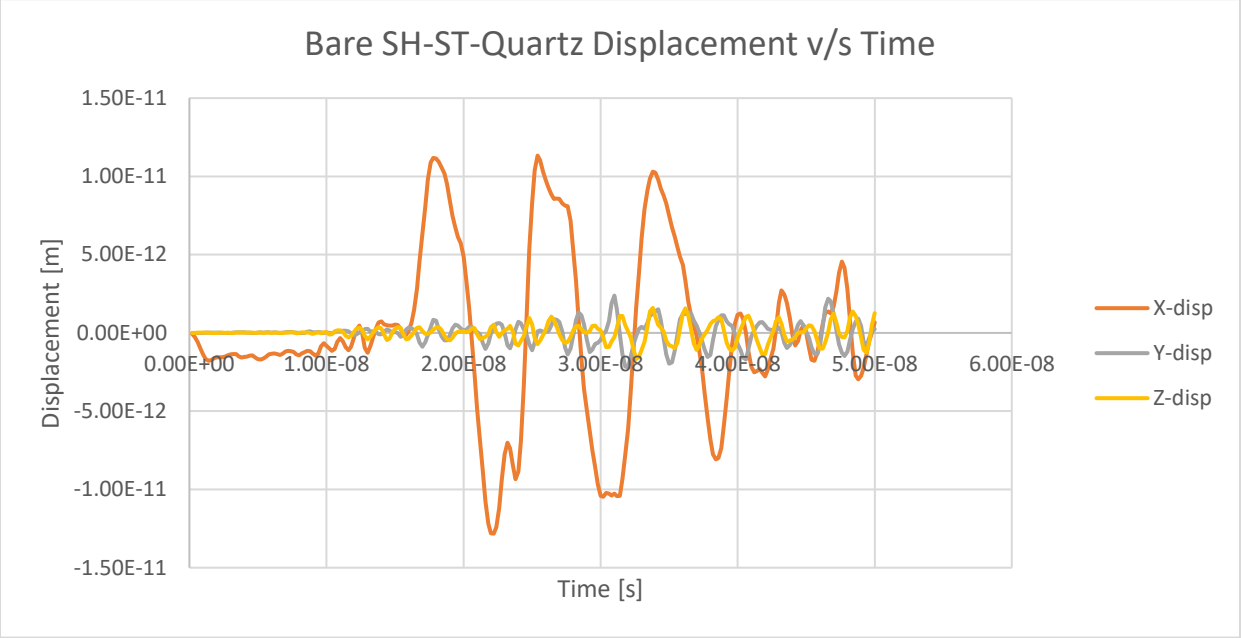

(a)

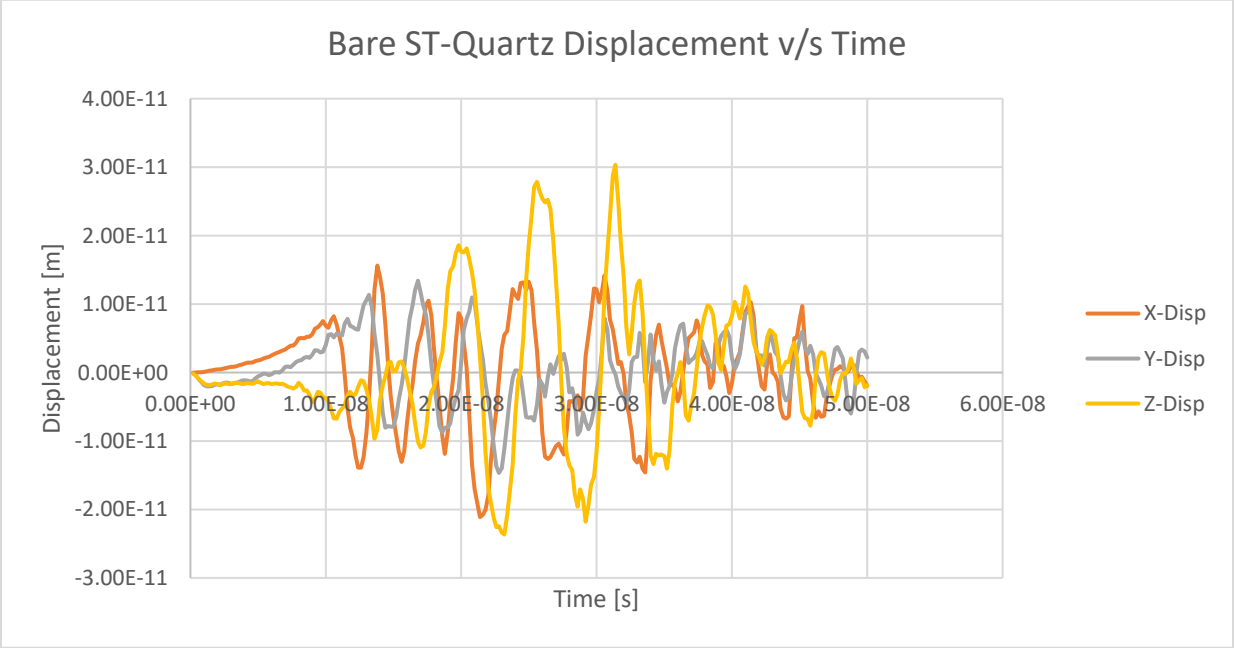

(b)

Figure 3.2 Displacement profiles of a node near the Cartesian origin of a bare ST-Quartz crystal. (a) The ST-Quartz crystal in the shear-horizontal mode. (b) The ST-Quartz crystal in the Rayleigh mode.

In Figure (3.2), the former figure represents the profiles of the bare ST-Quartz crystal in the SH-SAW mode, while the latter represents the RSAW mode. In the SH-SAW mode, the *x*-displacement is the largest, as is characteristic of shear-horizontal leaky SAW. Figure (3.3) shows the *x*-displacements of a node near the Cartesian origin for two models with different wavelengths. The model with the shorter wavelength produced a wave with a higher frequency, as expected. Moreover, the onset of the wave with the higher wavelength took a longer time, due to a larger distance. This indicated the necessity for scaling the sampling time and frequency of all models according to their wavelengths, to be able to capture waveforms with comparable fidelities.

3.1.3 Love Wave Velocity Profiles

For the bare ST-Quartz chip, the SH-SAW has a reported wave velocity of 5100 m/s [44]. In Figure (3.4) below, the wave velocity for zero-layer-thickness models agrees with the reported velocity, while they decrease with an increasing layer thickness.

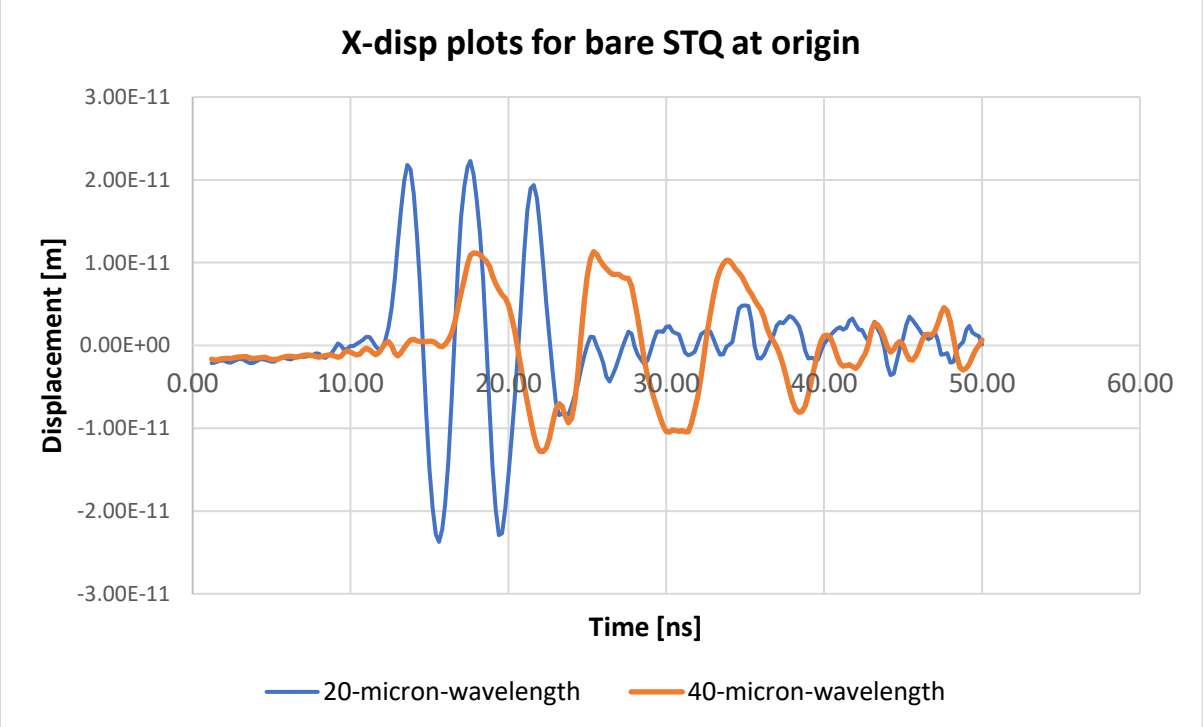

Figure 3.3 X-displacement profiles for bare ST-Quartz in the shear-horizontal mode with 20- and 40-micron wavelengths.

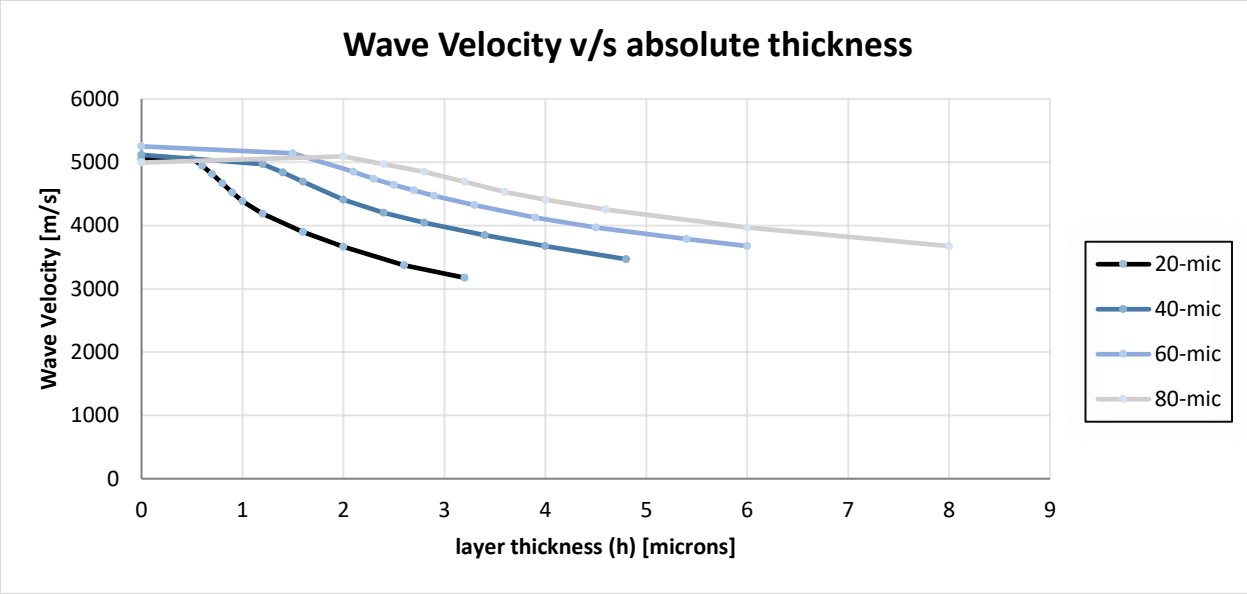

(a)

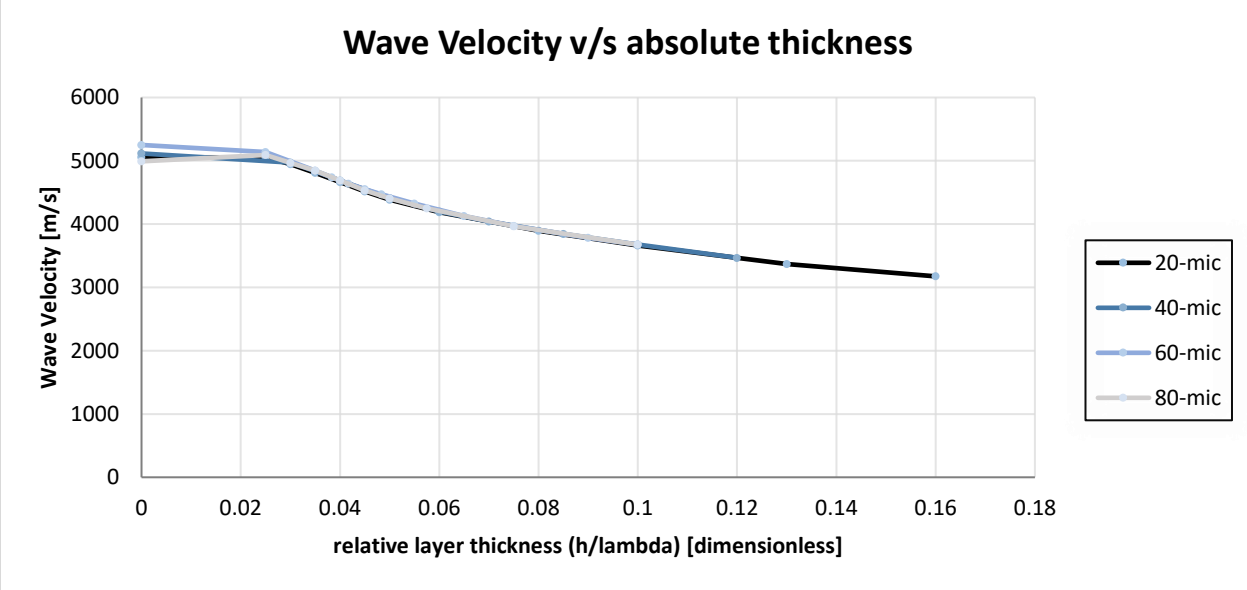

(b)

Figure 3.4 Wave velocity profiles for Love wave models with different wavelengths and ZnO layer thicknesses. (a) X-axis showing absolute layer thicknesses, in microns. (b) X-axis showing relative layer thicknesses.

For the bare ST-Quartz chip, the sensitivity values were a little unreliable, since obtaining a strong SH-SAW signal on the surface was unexpected to begin with. However, as the guiding layer was introduced, the signal picked up and the sensitivity improved manifold.

3.2 Sensitivity Results

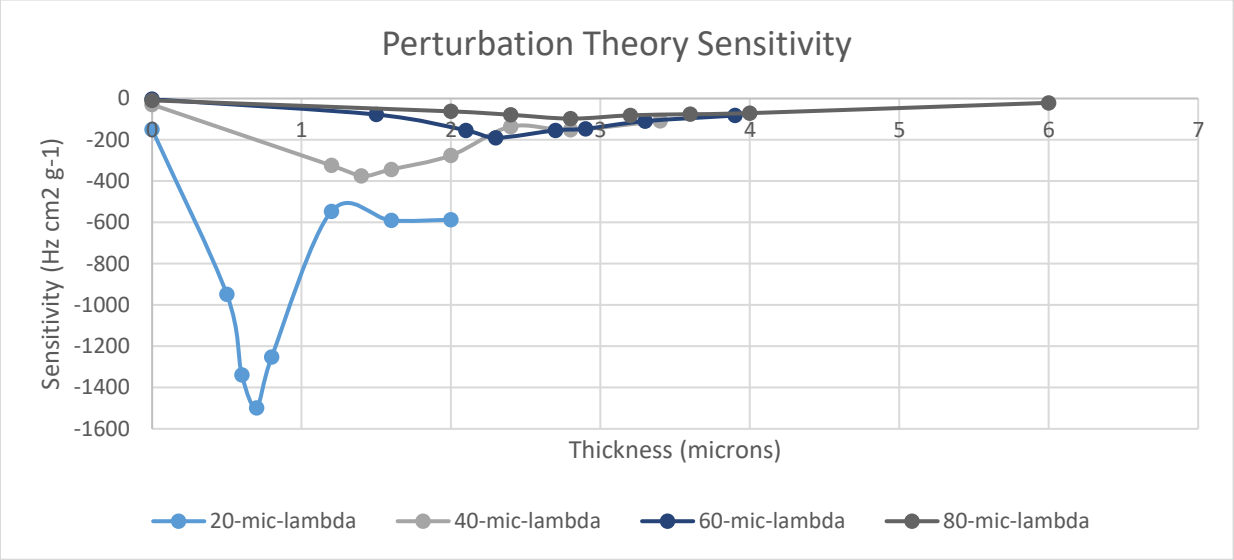

(a)

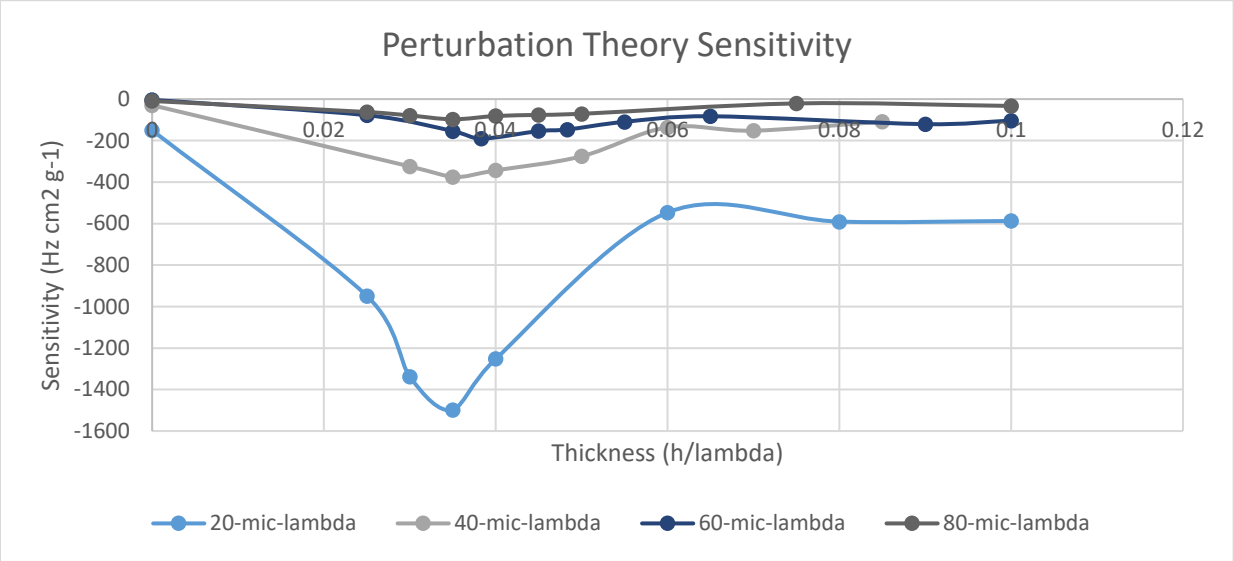

(b)

Figure 3.5 Sensitivity for Love wave models with different wavelengths and ZnO layer thicknesses. (a) Sensitivity plotted against absolute layer thicknesses, in microns. (b) Sensitivity plotted against relative layer thicknesses.

Figure (3.5) shows the plots of sensitivity against ZnO layer thicknesses. From Figure (a), the model with the lowest wavelength, the 20-micron-lambda, outperformed all other models due to a variety of reasons. As has been reported previously, models with higher operational frequency

always outperform their lower-frequency counterparts. Moreover, since these models were geometrically scaled from the smallest model, the 20-micron-lambda model had the shortest delay path to the Cartesian origin, where the measurements were taken. Figure (3.5b) shows the same plot of sensitivity against relative thickness of ZnO. That plot shows peaks of models with different wavelengths manifesting their peak sensitivity at a similar relative thickness ratio, at h/lambda ≈ 0.035. The following Figure (3.6) shows the same plot as Figure (3.5b) but with -log(-Sensitivity) for better visualization of the peaks.

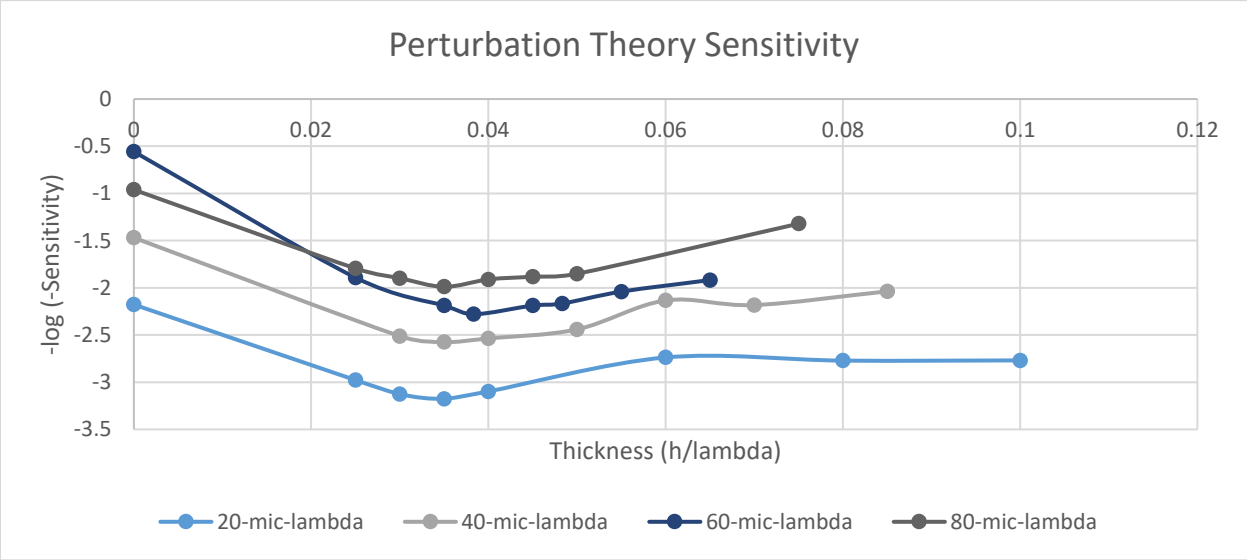

Figure 3.6 Log sensitivity plotted against relative layer thicknesses for Love wave models with different wavelengths and ZnO layer thicknesses.

From Figure (3.6), the optimal thickness for sensitivity can be said to be a relative parameter. For the ZnO/ST-Quartz configuration, the optimal thickness for the Love wave is around a ratio of 0.035 of h/lambda.

3.3 RSAW Results

Testing for RSAW capabilities with a ZnO/ST-Quartz system involved two configurations: one with the IDTs below the ZnO and another with the IDTs above the ZnO layer. The wavelength

used for the RSAW model was 20 microns. The power spectra were plotted in response to the same impulse testing that was performed for Love wave models previously.

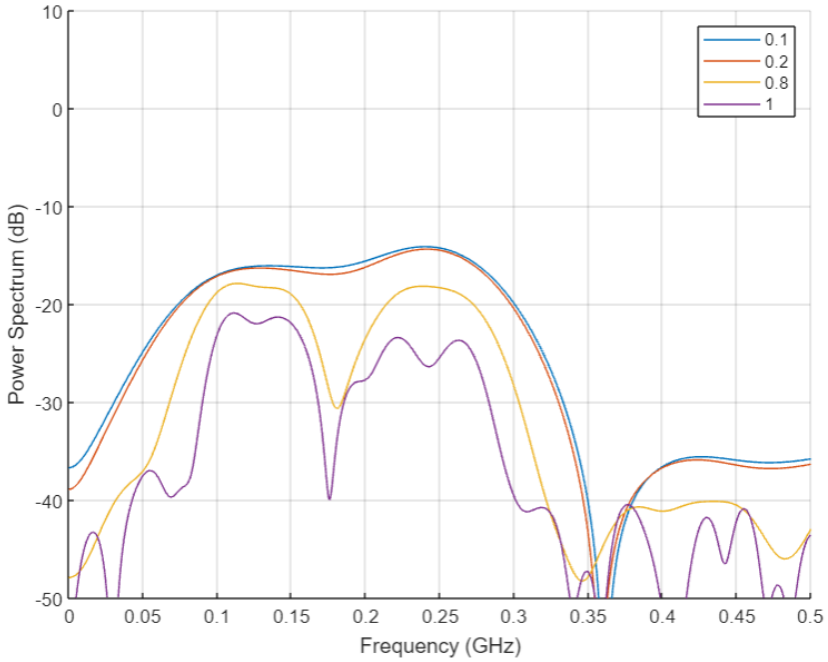

(a)

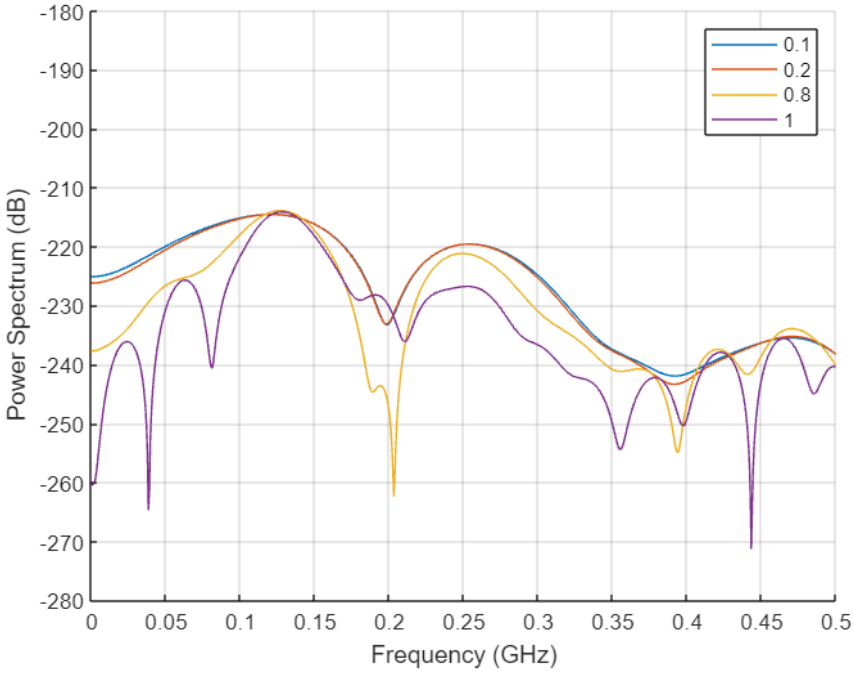

(b)

Figure 3.7 Power spectra for RSAW models with a 20-micron ZnO layer thickness and 20-micron wavelength IDTs above the guiding layer. (a) Voltage and (b) *z*-displacement power.

An example of the RSAW spectrum is shown in Figures (3.7a) and (3.7b) above. Two peaks can be observed in both figures, which correspond to the expected frequencies of the ST-Quartz substrate (lower frequency) and the ZnO guiding layer (higher frequency). The two voltage power peaks have comparable energy; however, the z-displacement peak from the substrate dominates its counterpart.

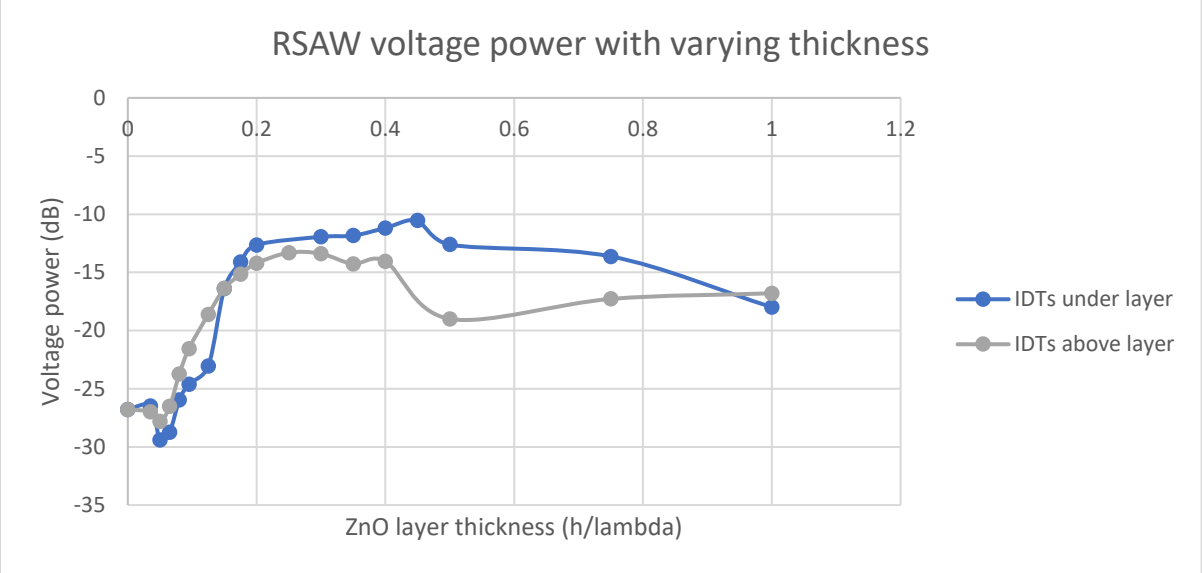

(a)

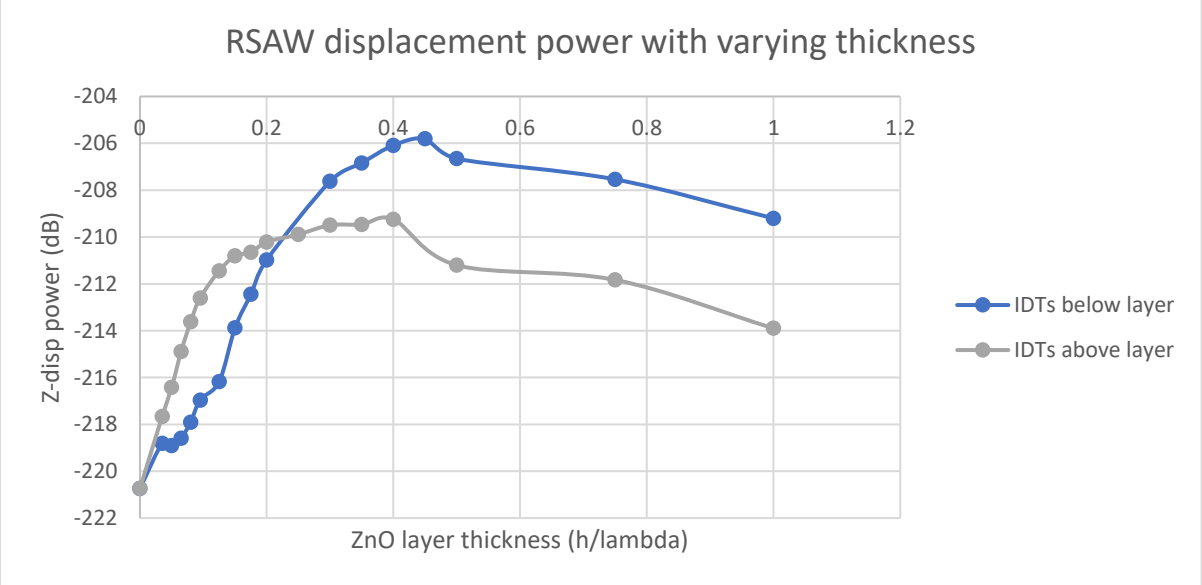

(b)

Figure 3.8 Impulse-response power plotted against relative ZnO layer thicknesses for RSAW models with a 20-micron wavelength. (a) Voltage power and (b) z-displacement power.

Figures (3.8a) and (3.8b) show the plots of voltage and displacement power with varying ZnO thickness. In both cases of measured power, the IDT configuration on top of the guiding layer initially fared better than that below the guiding layer. However, the IDTs below the guiding layer showed the maximum values for both types of power. A possible explanation for this phenomenon could be that a "sandwiched" configuration of IDTs optimizes contact surface area of the transducers. In both IDT configurations, the resonant voltage frequency kept switching back and forth from the typical ST-Quartz wave velocity to that of a ZnO layer, as shown in Table (3.1) below. In contrast, the resonant z-displacement frequencies decreased monotonically from the typical ST-Quartz RSAW frequency for a wavelength of 20 microns with both IDT configurations.

Table 3.1 Resonant frequencies for ZnO/ST-Quartz RSAW modeling. Wavelength of the model was 20 microns, with IDTs sandwiched between the substrate and guiding layer.

Guiding layer thickness (microns)	Relative (h/lambda)	Peak voltage (MHz)	Peak z-displacement (MHz)
0	0	194.75	163
0.7	0.035	211.84	163
1	0.05	157.51	161.78
1.3	0.065	158.73	161.17
1.6	0.08	162.39	159.34
1.9	0.095	162.39	158.12
2.5	0.125	163.61	156.29
3	0.15	251.53	153.58
3.5	0.175	244.81	151.4
4	0.2	241.15	149.57
6	0.3	230.77	143.47
7	0.35	139.8	140.42
8	0.4	137.97	137.97
9	0.45	135.53	133.7
10	0.5	132.48	128.82
15	0.75	134.31	120.27
20	1	134.31	119.66

The dominant frequency switching for voltage power may be attributed to constructive and destructive interference between the voltage waves actuated by both materials from the same set of IDTs. However, for the z-displacement power from the ST-Quartz substrate seemed to dominate even in configurations where the IDTs were on top of the guiding layer. This explains why the switching did not occur for the z-displacement power. Nevertheless, the guiding layer improved signal power in all cases when compared to the bare ST-Quartz device. An optimal ZnO relative thickness (h/lambda) was observed to be around 0.4 for RSAW, about twelve times that observed for the Love wave.

Chapter 4: Conclusion, Drawbacks, and Future Work

This Chapter is divided into two parts: 1) the main conclusion based on the previous chapter, and 2) drawbacks and suggested improvements for the future.

4.1 Conclusion

In Chapter 3, the validity of the Love wave and RSAW models was established, and the results were presented. For the Love wave simulations, it was observed that the addition of a ZnO guiding layer to the bare ST-Quartz chip was beneficial for improving the sensitivity of the device. The sensitivity had a clear peak for a thickness to wavelength ratio of 0.035 for models with different wavelengths, and this peak grew exponentially higher with decreasing wavelengths. In all cases, the models with a guiding layer performed better than their bare ST-Quartz counterparts for the same wavelength.

For RSAW simulations, two IDT configurations were compared: one with the IDTs below the guiding layer and another with IDTs above the guiding layer. The voltage and displacement power spectra were plotted for models with varying ZnO thicknesses. From these spectra, the peak voltage and *z*-displacement power was measured for every thickness value and both IDT configurations. The best configuration was found to be that with IDTs below the guiding layer, with a thickness to wavelength ratio of 0.4.

Considering both results, a table of optimal configurations of an orthogonal device has been provided below (Table (4.1)). Note that optimal in this case refers to best sensitivity for the Love wave model, and the highest power for the RSAW model.

For a practical device, the sensitivity of the device would be more favorable over the optimal RSAW power delivery, because power can always be modulated from the external electrical sources.

Table 4.1 Sample design parameters for orthogonal ZnO/ST-Quartz sensor. The calculations are based on the optimal thickness/lambda ratios for the Love and Rayleigh waves, 0.035 and 0.4, respectively.

Love wave wavelength (microns)	Layer thickness (microns)	RSAW wavelength (microns)
20	0.7	1.75
40	1.4	3.5
60	2.1	5.25
80	2.8	7

4.2 Drawbacks and Future Work

4.2.1 Crystal Modeling

The mathematics behind crystal rotations and their corresponding material properties assume that the crystals are cubic in nature [27]. However, neither ST-Quartz nor ZnO are cubic in nature. The rotations may yield different material properties than those in reality.

4.2.2 Spatial and Temporal Resolution

Although the temporal resolution was selected to be much higher than the Nyquist rate for the impulse response models (refer to Chapter 2.1.1), the same was not true for spatial resolution. The number of nodes for the bare ST-Quartz substrate was about 220,000, while the number of elements was 160,000. Even with current specifications, a full results set for nodal displacement and voltage data reached sizes around 50 GBs. For designing a model capable of detecting higher order harmonic waves, such as a Sezawa wave, a much finer mesh would be needed, with higher computational and memory requirements.

4.2.3 IDT Offset

In preliminary simulations, it was observed that the sensitivity peaks would shift in terms of relative layer thickness when the offset between IDTs changed. Therefore, the applicability of the results herein to practical devices needs to be tested empirically.

4.2.4 Material Properties in Practice

The deposition of guiding layers with vacuum or chemical processes can imbue materials with a range of physical properties that depend on the processing conditions. An example of this can be seen in the variation of ZnO properties reported by Sharma et al. [45]. Such variations can affect the optimal configuration of layer-guided devices.

References

1. Vellekoop, M. J. (1998). Acoustic wave sensors and their technology. *Ultrasonics*, *36*(1–5), 7–14. https://doi.org/10.1016/S0041-624X(97)00146-7

2. Kinsley, T., Lambert, T. M., Schwartz, D., Armstrong, J. H., Baerwald, H. G., Harvey, R. L., … Wentworth, J. W. (1972). IRE Standards on Piezoelectric Crystals: Measurements of Piezoelectric Ceramics, 1961*, *1962*(Reaffirmed).

3. Campbell, C. (2012). *Surface acoustic wave devices and their signal processing applications*. Elsevier.

4. Huang, Y., Das, P. K., & Bhethanabotla, V. R. (2021). Surface acoustic waves in biosensing applications. *Sensors and Actuators Reports*, *3*, 100041.

5. Ieki, H., Tanaka, H., Koike, J., & Nishikawa, T. (1996, June). Microwave low insertion loss SAW filter by using ZnO/sapphire substrate with Ni dopant. In *1996 IEEE MTT-S International Microwave Symposium Digest* (Vol. 2, pp. 409-412). IEEE.

6. Avramov, I. D., Voigt, A., & Rapp, M. (2005). Rayleigh SAW resonators using gold electrode structure for gas sensor applications in chemically reactive environments. *Electronics Letters*, *41*(7), 450-452.

7. Rulf, B. (1969). Rayleigh waves on curved surfaces. *The Journal of the Acoustical Society of America*, *45*(2), 493-499.

8. Sansone, L., Macchia, E., Taddei, C., Torsi, L., & Giordano, M. (2018). Label-free optical biosensing at femtomolar detection limit. *Sensors and Actuators, B: Chemical*, *255*, 1097–1104. https://doi.org/10.1016/j.snb.2017.08.059

9. Janeway Jr, C. A., Travers, P., Walport, M., & Shlomchik, M. J. (2001). The interaction of the antibody molecule with specific antigen. In *Immunobiology: The Immune System in Health and Disease. 5th edition*. Garland Science.

10. Länge, K., Rapp, B. E., & Rapp, M. (2008). Surface acoustic wave biosensors: a review. *Analytical and bioanalytical chemistry*, *391*(5), 1509-1519.

11. Klueh, U., Liu, Z., Feldman, B., Henning, T. P., Cho, B., Ouyang, T., & Kreutzer, D. (2011). Metabolic biofouling of glucose sensors in vivo: Role of tissue microhemorrhages. *Journal of Diabetes Science and Technology*, *5*(3), 583–595. https://doi.org/10.1177/193229681100500313

12. Richardson, M., Das, P. K., Morrill, S., Suthar, K. J., Sankaranarayanan, S. K., & Bhethanabotla, V. R. (2022). Removal of Non-Specifically Bound Proteins Using Rayleigh Waves Generated on ST-Quartz Substrates. *Sensors*, *22*(11), 4096.

13. Singh, R., Sankaranarayanan, S. K. R. S., & Bhethanabotla, V. R. (2009). Orthogonal surface acoustic wave device based on langasite for simultaneous biosensing and biofouling removal. *Applied Physics Letters*, *94*(26), 10–13. https://doi.org/10.1063/1.3160735

14. Hickernell, F. S., & Adler, E. L. (1997). Experimental and theoretical characterization of SAW modes on ST-X quartz with a zinc oxide film layer. *Proceedings of the Annual IEEE International Frequency Control Symposium*, (2), 852–857. https://doi.org/10.1109/freq.1997.639202

15. Cular, S., Branch, D. W., Bhethanabotla, V. R., Meyer, G. D., & Craighead, H. G. (2008). Removal of Nonspecifically Bound Proteins on Microarrays Using Surface Acoustic Waves. *IEEE Sensors Journal*, *8*(3), 314–320. https://doi.org/10.1109/JSEN.2008.917478

16. Slawinski, M. A. (1996). *On elastic-wave propagation in anisotropic media: reflection/refraction laws, raytracing, and traveltime inversion*. University of Calgary, Department of Geology and Geophysics.

17. Wang, X., & Uchiyama, S. (2013). State of the art in biosensors-general aspects. *InTech, Published Online*.

18. Chu, S. Y., Water, W., & Liaw, J. T. (2003). An investigation of the dependence of ZnO film on the sensitivity of Love mode sensor in ZnO/quartz structure. *Ultrasonics*, *41*(2), 133–139. https://doi.org/10.1016/S0041-624X(02)00430-4

19. Zadeh, K. K., Trinchi, A., Wlodarski, W., & Holland, A. (2002). A novel love-mode device based on a ZnO/ST-cut quartz crystal structure for sensing applications. *Sensors and Actuators, A: Physical*, *100*(2–3), 135–143. https://doi.org/10.1016/S0924-4247(02)00038-9

20. Kovacs, G., Lubking, G. W., Vellekoop, M. J., & Venema, A. (1992). Love waves for (bio)chemical sensing in liquids. *Proceedings - IEEE Ultrasonics Symposium*, *1992-October*, 281–285. https://doi.org/10.1109/ULTSYM.1992.275995

21. Gaso, M. M. I. R., Jiménez, Y., Francis, L., & Arnau, A. (2013). Love wave biosensors: a review. *State Art Biosens. Gen. Asp*, 277-310.

22. Tutuncu, G., Forrester, J.S., Chen, J., Jones, J.L. (2017). Extrinsic contributions to piezoelectric Rayleigh behavior in morphotropic PbTiO3 - BiScO3. *Acta Materialia*. doi: 10.1016/j.actamat.2017.07.032

23. Hirata, K., Mori, Y., Yamada, H., Uehara, M., Anggraini, S. A., & Akiyama, M. (2021). Significant enhancement of piezoelectric response in AlN by Yb addition. *Materials*, *14*(2), 1–10. https://doi.org/10.3390/ma14020309

24. Yang, Y., Wang, X., Zeng, F., & Pan, F. (2008). Giant piezoelectric d33 coefficient in ferroelectric vanadium doped ZnO films. Applied Physics Letters. 92. 10.1063/1.2830663.

25. Li, S., Sankaranarayanan, S. K. R. S., Fan, C., Su, Y., & Bhethanabotla, V. R. (2017). Achieving Lower Insertion Loss and Higher Sensitivity in a SAW Biosensor via Optimization of Waveguide and Microcavity Structures. *IEEE Sensors Journal*, *17*(6), 1608–1616. https://doi.org/10.1109/JSEN.2017.2651102

26. Abdollahi, A., Jiang, Z., & Arabshahi, S. A. (2007). Evaluation on mass sensitivity of saw sensors for different piezoelectric materials using finite element analysis. *IEEE International Symposium on Applications of Ferroelectrics*, *54*(12), 734–737. https://doi.org/10.1109/ISAF.2007.4393386

27. Auld, B. A. (1973). *Acoustic fields and waves in solids*. Рипол Классик.

28. Wang, Z. J., Cheeke, D. N., & Jen, C. K. (1996). Perturbation method for analyzing mass sensitivity of planar multilayer acoustic sensors. *IEEE Transactions on Ultrasonics, Ferroelectrics, and Frequency Control*, *43*(5), 844–851. https://doi.org/10.1109/58.535485

29. Sajid, S., & Chouinard, L. (2019). Impulse response test for condition assessment of concrete: A review. *Construction and Building Materials*, *211*, 317-328.

30. Fall, D., Duquennoy, M., Ouaftouh, M., Piwakowski, B., & Jenot, F. (2015). Modelling based on spatial impulse response model for optimization of inter digital transducers (SAW sensors) for non destructive testing. *Physics Procedia*, *70*, 927-931.

31. Lam, C. S., Wang, C. Y., & Wang, S. M. (2010, March). A review of the recent development of temperature stable cuts of quartz for SAW applications. In Proceedings of the Fourth International Symposium on Acoustic Wave Devices for Future Mobile Communication Systems, Chiba, Japan (pp. 3-5).

32. Wang, J. L., Guo, Y. J., Long, G. D., Tang, Y. L., Tang, Q. B., Zu, X. T., ... & Fu, Y. Q. (2020). Integrated sensing layer of bacterial cellulose and polyethyleneimine to achieve high sensitivity of ST-cut quartz surface acoustic wave formaldehyde gas sensor. Journal of hazardous materials, 388, 121743.

33. Zerdali, M., Bechiri, F., Hamzaoui, S., Teherani, F. H., Rogers, D. J., Sandana, V. E., ... & Roussigné, Y. (2017, March). Identification of acoustic waves in ZnO materials by Brillouin light scattering for SAW device applications. In Oxide-based Materials and Devices VIII (Vol. 10105, pp. 180-190). SPIE.

34. Caliendo, C., & Hamidullah, M. (2016). A theoretical study of love wave sensors based on ZnO–glass layered structures for application to liquid environments. *Biosensors*, *6*(4), 59.

35. Mitsuyu, T., Ono, S., & Wasa, K. (1980). Structures and SAW properties of rf-sputtered single-crystal films of ZnO on sapphire. *Journal of Applied Physics*, *51*(5), 2464-2470.

36. Bond, W. L. (1943). The mathematics of the physical properties of crystals. *The Bell System Technical Journal*, *22*(1), 1-72.

37. Giurgiutiu, V. (2015). Fundamentals of Aerospace Composite Materials.[In] Structural Health Monitoring of Aerospace Composites. Chapter 2, p 30

38. Voigt, W. (1910). *Lehrbuch der kristallphysik:(mit ausschluss der kristalloptik)* (Vol. 34). BG Teubner

39. Ogi, H., Ohmori, T., Nakamura, N., & Hirao, M. (2006). Elastic, anelastic, and piezoelectric coefficients of α-quartz determined by resonance ultrasound spectroscopy. Journal of Applied Physics, 100(5), 053511.

40. Heyliger et al.: Elastic constants of natural quartz J. Acoust. Soc. Am., Vol. 114, No. 2, August 2003.

41. Silva, L. B., & Santos, E. J. (2012). Quartz transducer modeling for development of BAW resonators. change, 1, 2.

42. Klingshirn, C. (2007). ZnO: material, physics and applications. *ChemPhysChem*, *8*(6), 782-803.

43. Carlotti, G., Socino, G., Petri, A., & Verona, E. (1987). Acoustic investigation of the elastic properties of ZnO films. *Applied Physics Letters*, *51*(23), 1889-1891.

44. Morgan, D. (2010). *Surface acoustic wave filters: With applications to electronic communications and signal processing*. Academic Press.

45. Sharma, P., Guler, Z., & Jackson, N. (2021). Development and characterization of confocal sputtered piezoelectric zinc oxide thin film. *Vacuum*, *184*, 109930.